Article

PEGylated Terbium-Based Nanorods as Multimodal Bioimaging Contrast Agents

Carlos Caro, Jose M. Paez-Muñoz, Ana M. Beltrán, Manuel Pernia Leal,* and María Luisa García-Martín*

Read Online

ACCESS | Metrics & More | Article Recommendations | Supporting Information

ABSTRACT: Diagnostic imaging strongly relies on the use of contrast agents (CAs). In general terms, current CAs present undesirable side effects that encourage researchers and pharmaceutical companies to continually search for safer and more versatile alternatives. Here, we describe the synthesis and characterization of terbium-based nanorods (TbNRs) as a potential alternative to traditional CAs for magnetic resonance imaging (MRI) and X-ray computed tomography (CT). The paramagnetism and high atomic number of Tb provide TbNRs with both magnetic relaxivity and X-ray attenuation capabilities. After surface functionalization with a polyethylene glycol (PEG)-derived ligand, TbNRs showed high colloidal stability in physiological media. Additionally, toxicity studies conducted in cell cultures and zebrafish embryos demonstrated the safety of the as-synthesized TbNRs, thus supporting their potential use as CAs. Lastly, *in vivo* imaging experiments in mice demonstrated that TbNRs produce remarkable contrast enhancement on both MRI and CT.

KEYWORDS: Rare-earth nanoparticles, terbium, MRI, CT, contrast agents, multimodal imaging
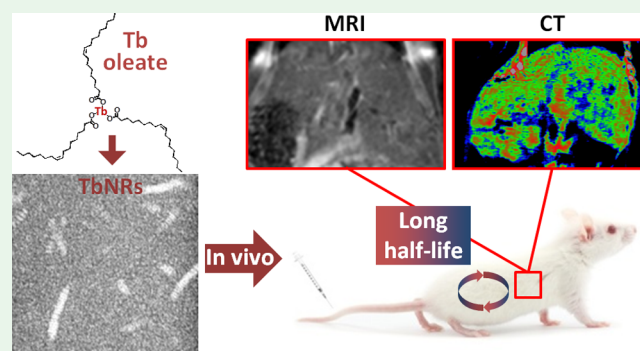
INTRODUCTION

Imaging-based diagnosis has long since become an essential tool for daily clinical practice. Among the different *in vivo* imaging modalities, MRI and CT stand out for their ability to render detailed 3D anatomical information along with functional information, especially in the case of MRI.[1] Although the use of contrast agents (CAs) is often unnecessary, in certain situations, they are essential for the proper visualization of a particular region of interest or to get relevant functional information, such as perfusion or diffusion parameters.[2] The most commonly used intravenous CAs are gadolinium- and iodine-based compounds for MRI and CT, respectively.[3,4] Gd chelates are routinely used as MRI CAs to generate positive contrast in T_1-weighted images as a result of shortening the longitudinal relaxation time (T_1) produced by the Gd cations on the protons of the nearby water molecules. As for iodine derivatives, they are used as CT CAs owing to the high atomic number of iodine ($Z = 53$), which strongly correlates with the X-ray attenuation coefficient. Image contrast in CT is produced by differences in the X-ray attenuation of tissues and, therefore, the presence of iodine derivatives will potentiate image contrast by increasing the attenuation coefficient of the tissues where they accumulate.[5] Although Gd chelates and iodinated compounds are still widely used at present, they have some important limitations.

On the one hand, Gd chelates can produce toxic effects caused by the unexpected release of Gd^{3+} and subsequent accumulation in different tissues,[6−8] whereas iodinated compounds can cause allergic reactions, contrast-induced nephropathy, or hyperthyroidism.[9−11] On the other hand, both types of CAs exhibit short blood half-lives since they are rapidly excreted by renal filtration due to their small size and, therefore, their use is limited to applications in which long circulation times are not required.

Current advances in medical imaging aim to increase diagnostic accuracy through different strategies, such as multimodal imaging evaluations. In this scenario, nanomedicine plays a key role, thanks to the enormous possibilities it offers to produce new nanoscale materials with improved properties and functionalities.[12] Thus, numerous new nanoscale CAs with great potential to improve the diagnostic accuracy of MRI and CT have been produced over the past few years.[13,14] Among them, nanostructures based on rare earth
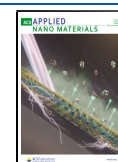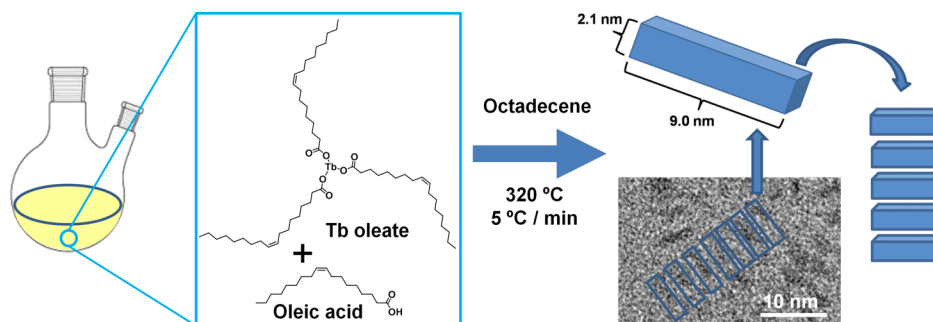
Scheme 1. Synthesis Procedure of TbNRs

(RE) elements have attracted a great deal of attention because of their unique physicochemical properties, which provide them with great potential for bioimaging applications.[15] Thus, the outstanding magnetic properties of several RE elements, such as Gd, Ho, Dy, or Tb, have been exploited for the development of a new generation of nanostructured CAs for MRI.[16−24] Likewise, lanthanide-based nanostructures are also suitable for CT imaging, thanks to the high atomic number (Z) of these elements, which allows them to efficiently absorb X-rays.[25,26] The vast majority of these studies use the lanthanide as a dopant agent and not as the main component of the nanostructured material. Yet, other RE-based structures, mostly lanthanide oxide nanoparticles (NPs), have also been explored as CAs for *in vivo* imaging. Among them, Gd-oxide NPs as MRI CAs are the most widely studied.[27−30] Regarding Tb-oxide NPs, Marasini *et al.*[31] recently reported the synthesis of ultrasmall paramagnetic NPs based on several lanthanide oxides, including Tb oxide. This work shows the potential of these NPs as MRI CAs, although no *in vivo* evidence has been reported so far. Indeed, it is worth noting here that a key aspect lacking in many of these studies is detailed *in vivo* characterization that demonstrates the real potential of these nanostructures as CAs. In addition to high biocompatibility, NP-based CAs must be able to escape the mononuclear phagocyte system and remain in circulation long enough to efficiently reach their target, especially in tumor imaging. However, many of the RE-based CAs, particularly those that use RE elements as the doping agent, exhibit large hydrodynamic diameters (HDs), usually above 100 nm, which *in vivo* lead to rapid liver uptake, limiting their applicability as CAs.[23,29,32] On the other hand, long circulation times are determined not only by the size of the NPs but also by their coating. In this regard, stealth polymers such as polyethylene glycol (PEG) have been shown to efficiently prolong blood circulation times.[33] Here, we report the synthesis of terbium-based nanorods (TbNRs) with sizes of 2 × 9 nm with high colloidal stability and excellent luminescent, magnetic, and X-ray attenuation properties. These TbNRs were well dispersed in physiological medium by a simple ligand exchange with a catechol-derived PEG ligand. The cytotoxicity of the resulting PEGylated TbNRs (PEG−TbNRs) was assessed *in vitro* using different assays, including MTT, live-dead, and flow cytometry, and *in vivo* using zebrafish embryos. Then, *in vivo* imaging studies were conducted in mice to determine the suitability of PEG−TbNRs as CT and MRI CAs.

■ EXPERIMENTAL SECTION

Materials. Commercial reagents and solvents were purchased from accredited suppliers (Sigma-Aldrich, Fisher Scientific, and Acros Organics): terbium(III) chloride, oleic acid 99%, sodium oleate, 1-octadecene, PEG, gallic acid, 4-dimethylaminopyridine, triethylamine, dicyclohexylcarbodiimide (DCC), nitric acid (HNO_3), sodium sulfate (Na_2SO_4), hydrochloric acid (HCl), 3-[4,5-dimethylthiazol-2yl]-2,5-diphenyl tetrazolium bromide (MTT), Triton X-100, TO-PRO-3 iodine, DAPI (4′,6-diamidino-2-phenylindole), Roswell Park Memorial Institute (RPMI) medium, and phosphate buffered saline (PBS). The solvents: ethanol, toluene, chloroform, hexane, acetone, dimethylsulphoxide (DMSO), tetrahydrofuran, and dichloromethane were used in the anhydrous form and with HPLC grade; Milli-Q water was used (Millipore, filter pore size 0.22 μM, 18.2 MΩ).

Synthesis of TbNRs. *Synthesis of Tb Oleate.* For the synthesis of Tb oleate, we used an adapted version of the protocol reported by Liu *et al.*[24] In brief, a mixture of 1.87 g of terbium chloride (7.05 mmol) and 4.75 g of sodium oleate (15.60 mmol) was dissolved in 7 mL of distilled water, 10 mL of ethanol, and 17 mL of hexane. This solution was refluxed for 4 h under an inert atmosphere, cooled to room temperature and transferred into a separation funnel. The organic layer, which contains the desired terbium oleate, was washed several times using distilled water. The hexane was evaporated using a rotavapor.

Synthesis of TbNRs. A total of 0.511 g (0.51 mmol) of terbium oleate, along with 0.250 g (0.89 mmol) of oleic acid and 3.5 mL of 1-octadecene was heated at 320 °C for 1 h in an inert atmosphere (Scheme 1). Then, the mixture was cooled down to room temperature and washed several times with a mixture of ethanol and acetone (1:1) as precipitating agents, and subsequently centrifuged (10 min at 5.000 rpm). TbNRs were then resuspended in toluene.

Functionalization of TbNRs. The detailed procedure concerning the ligand synthesis is described in the Supporting Information. In brief, a solution containing 1.0 mL of TbNRs (10 g/L), 1.0 mL of the ligand GA-PEG3000-OH (0.1 M in $CHCl_3$), and 50 μL of triethylamine was put in a separating funnel. This mixture was shaken gently and then diluted by adding 5 mL of toluene, 10 mL of acetone, and 5 mL of Milli-Q water. Subsequently, this mixture was shaken, the aqueous layer collected in a round-bottom flask, and the remaining organic solvents rotaevaporated. The resulting water-soluble PEG−TbNRs were purified using 100 kDa cut-off centrifuge filters at 450 rcf until the free ligand was completely removed. Then, the PEG−TbNRs were diluted in the corresponding media and centrifuged during 5 min at 150 rcf.

Characterization. *Transmission Electron Microscopy.* Transmission electron microscopy (TEM) and scanning-TEM (STEM) images were obtained on a FEI TALOS F200 (FEI, Hillsboro, OR, USA) operating at 200 kV accelerating voltage and equipped with Super-X energy-dispersive X-ray spectrometry (EDX). Compositional analyses of the samples were performed by the combination of high-angle annular dark-field images (HAADF) and EDX acquisitions in TEM and STEM modes (0.2 s dwell time and spatial drift correction). Sample preparation consisted of dropwise adding TbNR solution (~1 g/L of Tb) onto a carbon-coated copper grid and letting it dry. The length and diameter of TbNRs were calculated as the average of a hundred TbNRs measured.
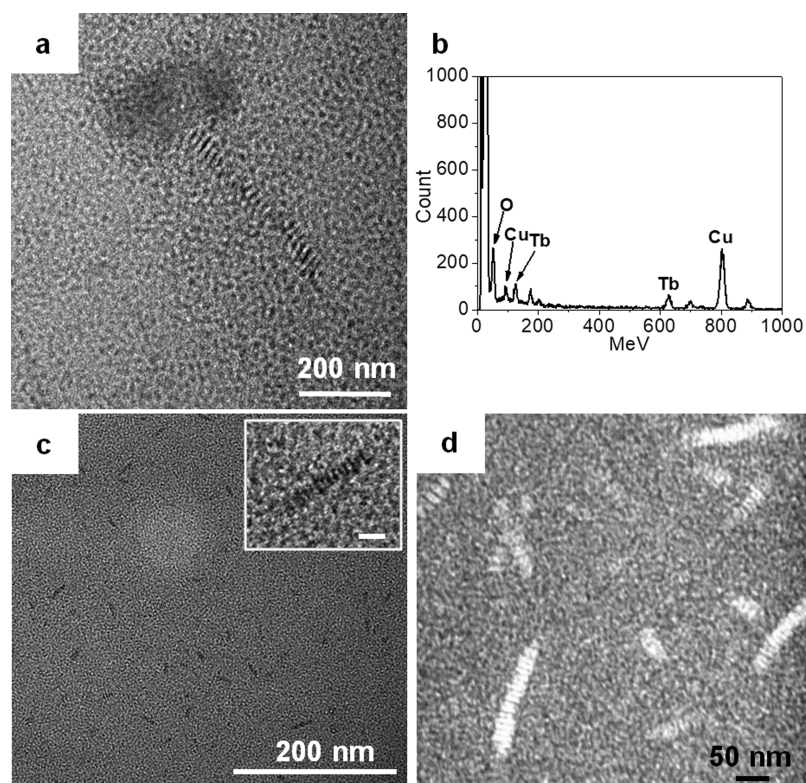
Figure 1. TEM (a) and EDX (b) images of TbNRs before functionalization. TEM (c) and STEM (d) images of PEGylated TbNRs. Inset shows a higher-magnification image (scale bar corresponds to 10 nm).

UV−vis Spectroscopy. The UV−vis spectra were registered on a Cary 100 (Agilent, Waltham, MA, U.SA) spectrometer using a quartz tray with 1 cm light path.

Fluorescence Spectroscopy. The fluorescence spectra were recorded with an Edinburgh Instruments FLS920 (Edinburgh, U.K) spectrometer with a quartz tray (light path = 1 cm).

Vibrating Sample Magnetometer. The analysis of the magnetization behavior was performed on a vibrating sample magnetometer (VSM) (MicroMag 3900, Princeton Measurements Corp., U.SA) using magnetic fields ranging from −1 to 1 T at 5 and 300 K.

Dynamic Light Scattering. PEG−TbNR size distribution was analyzed using a Zetasizer Nano ZS90 (Malvern Instruments, Malvern, Worcestershire, U.K). PEG−TbNRs were dispersed in PBS or culture medium at a final concentration of 50 mg/L(Tb). ZEN0118-low-volume disposable sizing cuvettes were used for these measurements; 2.420 was set as the refractive index with an angle of detection of 173° backscatter (NIBS default). The measurement time was determined automatically. Three measurements were performed per sample. The size distribution was determined using the number mean. The analysis was done according to the general-purpose (normal resolution) model.

Fourier Transform Infrared Spectroscopy. Fourier transform infrared spectroscopy (FTIR) spectroscopy was performed on a JASCO FTIR-4100 equipped with an ATR accessory (MIRacle ATR, PIKE Technologies) coupled to a mercury cadmium telluride (MCT) detector cooled with liquid nitrogen. Spectra acquisition was performed from 4000 to 800 cm^{-1} (4 cm^{-1} resolution, 50 scans).

Nuclear Magnetic Resonance Spectroscopy. The ^{1}H NMR spectrum of the ligand prepared in CDCl$_3$ was acquired on a Bruker 400 MHz nuclear magnetic resonance (NMR) system (Bruker BioSpin, Rheinstetten, Germany).

Transversal Relaxivities (r$_2$). r_2 was measured in PBS at 1.44 and 9.4 T using concentrations of PEG−TbNRs ranging from 2 to 0.2 mM Tb. T_2 values at 1.44 T were determined on a Bruker Minispec MQ-60 (Bruker BioSpin, Rheinstetten, Germany) using a Carl−Purcell−Meiboom−Gill (CPMG) sequence. T_2 values at 9.4 T were

measured on a Bruker Biospec MRI spectrometer (Bruker Biospec, Bruker BioSpin, Ettlingen, Germany) equipped with a 40 mm quadrature resonator and 400 mT m^{-1} field gradients. T_2 values were measured using a 64-echo CPMG imaging sequence (TE values between 7.5 and 640 ms).

Transverse relaxivity, r_2, was determined as the slope of the linear fit of $1/T_2$ over [Tb].

Inductively Coupled Plasma High-Resolution Mass Spectroscopy. Tb concentration was determined on a NexION ICP−HRMS (PerkinElmer, Waltham, MA, U.SA). In brief, 25 μL of the TbNR solution was diluted with 2.5 mM aqua regia. This mixture was left overnight and then diluted up to 25 mL with water.

Cell Culture. N13 mouse microglial cells were grown in RPMI medium supplemented with 10% FBS, 2 mM L-glutamine, and 1% penicillin/streptomycin at 37 °C and 5% CO$_2$.

Cytotoxicity. The cytotoxicity of PEG−TbNRs was assessed in N13 cells by the MTT assay (details are given in the Supporting Information).

Cell Morphology Studies. These studies were performed using a PerkinElmer operetta high content imaging system, which allowed us to evaluate cell morphology and calculate the percentage of cell death. Further details are given in the Supporting Information.

Teratogenicity Assay. Wild-type zebrafish were used for these experiments. At day 0, they were outcrossed, and then, the embryos were collected and incubated in E3 medium for 4 h at 28 °C. Unfertilized eggs were discarded. Those embryos that developed properly were exposed to different concentrations of PEG−TbNRs in E3 medium. Eggs were deposited in eight-well Petri dishes (∼30 eggs in 4 mL). The hatching rate, malformations, and survival were analyzed at 24, 48, and 96 h of PEG−TbNRs exposure.

Animals. BALB/c mice (male, *ca.* 22 g weight, *n* = 3), provided by Janvier Labs (Le Genest-Saint-Isle, France), were used in all *in vivo* imaging experiments. The experiments were carried out in accordance with our local ethics committee guidelines and were consistent with the national regulations for the use and care of experimental animals (R.D. 53/2013). Prior to imaging experiments, mice were
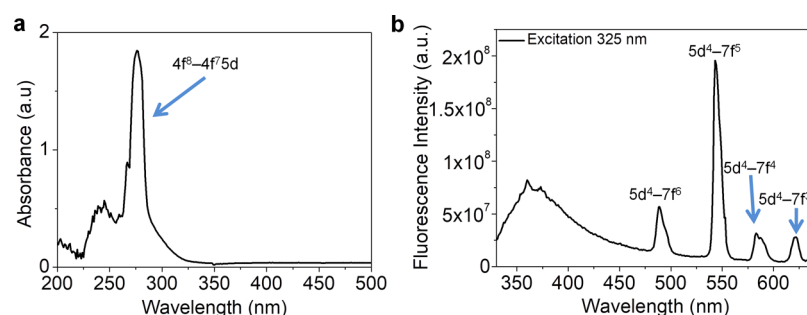
Figure 2. (a) UV−vis spectrum of PEG−TbNRs. (b) Fluorescence emission spectra of PEG−TbNRs.

anesthetized (1% isoflurane), and a catheter was introduced into their tail vein for intravenous administration of the PEG−TbNRs. Then, the animals were transferred to the imaging system (CT or MRI). The PEG−TbNRs were administered intravenously (10 mg of Tb per kg).

In Vitro and In Vivo CT. CT images were obtained on a Bruker Albira system (Bruker Biospec, Bruker BioSpin, Ettlingen, Germany) using the following parameters: 35 μm X-ray focal spot size (nominal), 45 kVp energy, working at 400 μA. Attenuation values were expressed in Hounsfield units, with the scale adjusted to better visualize soft tissues, overexposing the bones. Liver and kidney pharmacokinetics were calculated from the average values within the same regions of interest (ROIs) at different experimental times.

In Vivo MRI. MRI studies were performed on the 9.4 T Bruker Biospec system described in the Transversal relaxivities section by following the protocol described by us elsewhere.[34] In brief, high-resolution T_2-weighted images and a sequence of fast T_2-weighted images were acquired and analyzed to characterize the short-term pharmacokinetics (first 30 min). Then, quantitative T_2 maps were acquired at 0, 1, 24, 48, and 168 h to evaluate long-term biodistribution and pharmacokinetics.

Histology. At 168 h postinjection of the PEG−TbNRs, mice were euthanized and the kidneys, spleen, and liver were collected. Tissue architecture was assessed by light microscopy of hematoxylin and eosin (H&E)-stained tissue sections. Details are provided in the Supporting Information.

Statistical Analysis. The SPSS package (SPSS Inc., Chicago, Illinois) was used for the statistical analysis. Differences between different experimental conditions were determined by student's *t*-test or one-way analysis of variance (ANOVA), with a significance level of 0.05.

■ RESULTS AND DISCUSSION

Synthesis, Characterization, and Functionalization of TbNRs. TbNRs were synthesized by thermal decomposition of terbium−oleate in the presence of oleic acid in 1-octadecene. The morphology and size of the synthesized TbNRs were examined by TEM and EDX. The as-prepared particles showed an elongated shape of around 9.0 nm in length and 2.1 nm in width. Interestingly, these elongated particles were organized in elongated superstructures of around 80.2 nm in length and 9.2 nm in width (Figures 1a and S1). The formation of these assemblies of NPs occurred during the synthesis process, likely due to the different reactivity along the rods. These assemblies of oleic acid-capped NPs were ligand exchanged by catechol-derived PEG ligands, resulting in water-soluble assemblies with a structure similar to that of the as-synthesized TbNRs, as shown in the TEM images. Therefore, the gentle ligand exchange procedure was not sufficient to disassemble the NPs, probably due to the high energy of interaction between them.

The as-prepared TbNRs were capped by oleic acid surfactants, giving a hydrophobic character to the nanomaterial. Thus, to make them biocompatible, TbNRs were transferred to aqueous media by following a previously reported ligand exchange method,[35] using a catechol-derived PEG−OH ligand. As previously shown, catechol anchors strongly interact with the iron oxide NP surface via their phenolic hydroxyl groups.[36] These anchors form a stable 5-membered ring complex with the Fe cation. Similarly, lanthanide catecholate complexes are likely formed from trivalent lanthanide cations and catechol-derived ligands. Then, the bi-dentate catechol anchor of the ligand would react with the Tb at the surface of the NRs forming a stable complex similar to the terbium−catecholate complex [Tb$_2$(cat)$_3$] produced in solution.[37,38]

Characterization of PEGylated TbNRs. PEG−TbNRs were thoroughly characterized by different physicochemical techniques to determine their morphology, size, optical properties, magnetic properties, and colloidal stability. The original morphology and sizes of the pristine NRs were preserved after ligand exchange, as confirmed by TEM and STEM (Figures 1c,d and S1). Moreover, the attachment of the PEGylated ligand to the surface of the TbNRs was confirmed by FTIR spectroscopy (Figure S2). Additionally, these functionalized TbNRs were very stable in water without any sign of precipitation over time, further confirming the success in incorporating the PEGylated ligands on the surface of the TbNRs. Further analysis by dynamic light scattering (DLS) showed the high stability of PEG−TbNRs in physiological media, specifically in PBS and cell culture medium. PEG−TbNRs showed HDs around 75 nm in PBS, and slightly lower (∼60 nm) in cell culture medium. After 24 h, the HDs of PEG−TbNRs increased by around 30% and then remained stable throughout the measurement time (1 week). This behavior demonstrates the stability of PEG−TbNRs in physiological media and also that no aggregates were formed during ligand exchange (Figure S3).

REs also show interesting optical properties, which are governed by the electron configuration and can be characterized by UV−vis and photoluminescence (PL) spectroscopy. Thus, the optical absorption in the UV region of REs can originate from transitions 4f → 5d. Therefore, the peak observed at 277 nm in the UV−vis spectrum could be assigned to the 4f^8 → 4f^7 5d transition, which normally appears at more than 200 nm in the case of Tb ions (Figure 2).[39] The PL emission spectrum of the TbNRs dispersed in toluene at room temperature is shown (Figure 2). The emission spectrum of TbNRs under 325 nm excitation displayed four emission peaks, which could be assigned to the electron transitions from 5D^4 → 7F^6 (490 nm), 5D^4 → 7F^5 (546 nm), 5D^4 → 7F^4 (583 nm), and 5D^4 → 7F^3 (620 nm). Among these transitions, the green emission (546 nm) appeared as the strongest, which is in agreement with the Judd−Ofelt theory.[24]

Additionally, PEG−TbNRs were evaluated as potential CAs for *in vivo* imaging, specifically for CT and MRI. The ability of
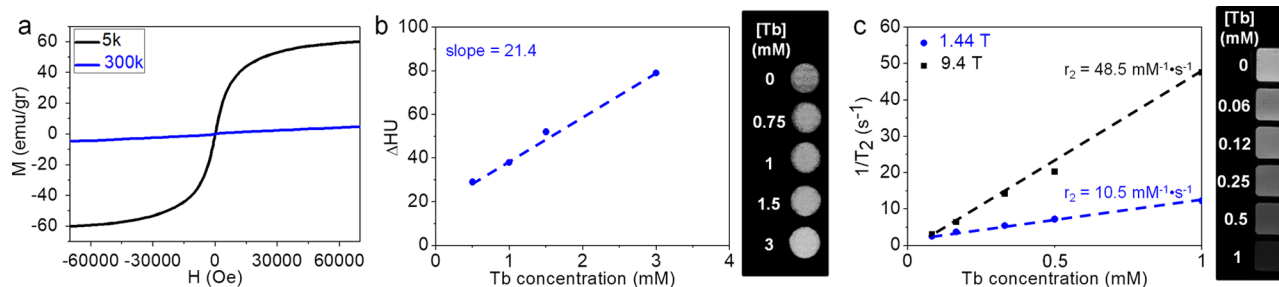
Figure 3. (a) hysteresis loop of PEG-TbNRs measured at 5 K (black) and 300 K (blue); (b) X-ray attenuation measured as the linear relationship between the intensity of the CT images and the concentration of Tb in the PEG−TbNR solutions; (b); (c) relaxation rate $(1/T_2)$ *vs* the concentration of Tb in the PEG−TbNR solutions measured at 1.44 T (black dots) and 9.4 T (red dots), and the linear fits (black and red lines) whose slopes correspond to the transverse relaxivities (r_2) of PEG−TbNRs at both magnetic fields.
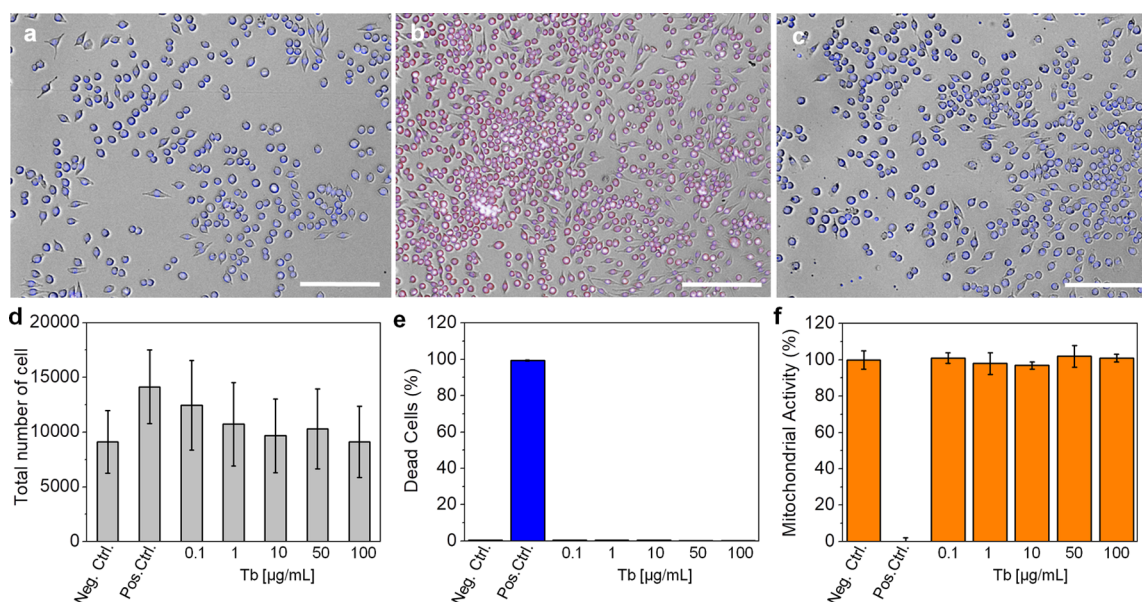

Figure 4. Optical microscopy images of N13 cells: (a) negative control, (b) positive control, (c) cells exposed PEG−TbNRs (100 μg/mL). Images correspond to the merging of TO-PRO-3 iodine (red), DAPI (blue), and bright field (gray). Scale bars correspond to 100 μm. Bar charts correspond to (d) total number of cells/well, (e) percentage of dead cells, and (f) cell viability (MTT assay) after exposure to increasing concentration of PEG−TbNRs for 24 h.

PEG−TbNRs to be used as CT CA was determined by measuring the X-ray attenuation. Interestingly, the slope of the linear fit of the X-ray attenuation *versus* the PEG−TbNRs concentration was 21.4 HU mM^{-1} [Tb], which is 10-fold higher than that obtained for the commercial CA iohexol (2.69 HU mM^{-1}) (Figure 3b).[40] On the other hand, the magnetic properties of PEG−TbNRs were studied to evaluate their potential as MRI CAs. First, the magnetic hysteresis loop measurements by the VSM showed that PEG−TbNRs exhibit superparamagnetic behavior at 5 K and paramagnetic at 300 K (Figure 3a). Then, their magnetic transverse relaxivity, r_2, was determined at 1.44 and 9.4 T. PEG−TbNRs showed r_2 values of 10.4 mM^{-1}•s^{-1} and 48.5 mM^{-1}•s^{-1} (Figure 3c) at low and high magnetic fields, respectively. Therefore, we can conclude that our PEG−TbNRs behave as multimodal imaging nanosystems for optical imaging, CT, and MRI. However, the emission wavelength of these PEG−TbNRs, around 540 nm, limits their applicability *in vivo* in optical imaging due to the high tissue autofluorescence at that wavelength,[41] together with weak tissue penetration. On the contrary, their excellent X-ray attenuation and magnetic relaxation properties make them very promising CT and MRI CAs for bioimaging.

***In Vitro* Cytotoxicity Assessment.** The evaluation of the cytotoxicity of new nanomaterials designed for biological applications is a crucial step that requires an exhaustive analysis. Therefore, we carried out a detailed analysis including multiple assays, namely, cell morphology, live-dead, and MTT assays. These assays were performed on the mouse microglial cell line, N13. After exposure to growing concentrations of PEG−TbNRs, from 0.1 to 100 μg/mL of Tb, N13 cells did not show evidence of morphological changes, even for the highest concentration evaluated (Figures 4a−c and S4). Furthermore, the total number of cells per well remained unaltered for all the concentrations tested (Figures 4d and S5). Indeed, the percentage of dead cells remained around 0%, without a statistically significant increase in all cases (Figures 4e and S5). Finally, no statistically significant effect on mitochondrial activity was observed with the MTT assay (Figure 4f). These results demonstrate that PEG−TbNRs exhibit excellent cellular biocompatibility, supporting their potential for *in vivo* applications. However, *in vivo* toxicity depends on many different factors that cannot be evaluated in cell cultures. Therefore, before proceeding with *in vivo* experiments on mice, toxicity was also assessed *in vivo* using zebrafish embryos.

Teratogenicity Assessment on Zebrafish Embryos. Teratogenicity of PEG−TbNRs was evaluated in zebrafish embryos, as previously described.[42] The survival and hatching rates of zebrafish embryos exposed to growing concentrations of PEG−TbNRs (0.1, 1, 10, 50, and 100 μg/mL of Tb) were assessed at different time points after fertilization. After 24 h postexposure, PEG−TbNRs were clearly observed to be interacting with the chorion of the embryos (Figure S6a). Regarding the hatching process, both control embryos and those exposed for 48 h to PEG−TbNRs showed 100% hatching (Figure S6b). These results agree with hatching rates reported for normal zebrafish embryos.[43] In addition, neither mortality nor malformations were observed at any time point in the embryos exposed to PEG−TbNRs (Figures 5 and S7).
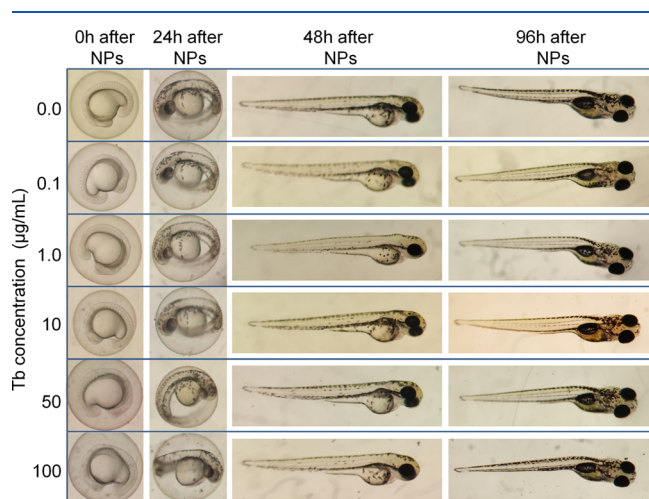

Figure 5. Morphological analysis of zebrafish embryos exposed to growing concentrations of PEG−TbNRs at different time points (24, 48, and 96 h).

***In Vivo* CT and MRI Studies.** CT imaging studies showed an increment of 5.5 ± 2.1 HU in the liver 1 h postadministration of PEG−TbNRs (10 mg of Tb per kg), which increased up to 12.1 ± 3.1 after 24 h (Figure 6). Then, the ΔHU values decreased, being 10.4 at 24 h and 6.1 at 168 h. Therefore, the maximal accumulation was detected at 24 h, and then, PEG−TbNRs were slowly cleared from the liver. Importantly, these results were obtained with an injection dose approximately 50 times lower than that recommended for
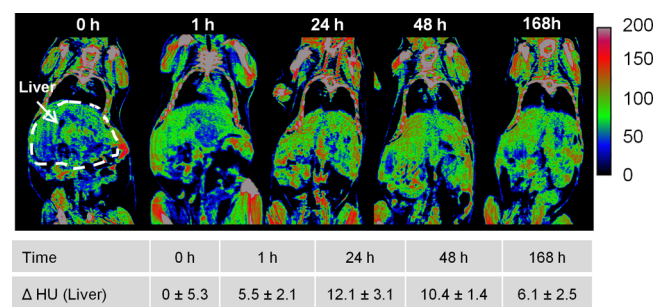

Time	0 h	1 h	24 h	48 h	168 h
Δ HU (Liver)	0 ± 5.3	5.5 ± 2.1	12.1 ± 3.1	10.4 ± 1.4	6.1 ± 2.5

Figure 6. Representative *in vivo* CT images at different time points (0, 1, 24, 48, and 168 h) after the injection of PEG−TbNRs. The liver has been highlighted for better visualization. Values are in Hounsfield units and the scale adjusted for better visualization of soft tissues, overexposing the bones.

iohexol, which is 430 mg per kilogram for body imaging applications.[44]

In vivo biodistribution and pharmacokinetics of the PEG−TbNRs were also evaluated by MRI. Short-term pharmacokinetics by dynamic T_2 imaging showed that the PEG−TbNRs were rapidly taken up by the liver, reaching a value of 50% of relative enhancement during the first 30 min after the intravenous administration of PEG−TbNRs (10 mg of Tb) (Figure 7a,b).

No significant accumulation was observed in the rest of the organs. Moreover, long-term pharmacokinetics showed a maximal T_2 decrease (ΔT_2 of 7.1 ms) at 24 h after administration, in agreement with the CT results shown above. A similar trend was observed in the kidneys, where the maximum T_2 decrease (ΔT_2 of 5.9 ms) was reached at 24 h. After 48 h, the kidneys recovered their initial T_2 values, whereas the liver only showed a slight T_2 recovery, in agreement with the slow liver clearance described in the CT studies (Figure 7c).

Quantitative Evaluation of Circulating Lifetime of PEG−TbNRs in the Bloodstream. Tb content in blood and the liver at 1 and 24 h was quantified by ICP−MS (Figure 8). The concentration of Tb in blood was 2.3 and 1.4 mg/L at 1 and 24 h postadministration, which corresponds to 10 and 6% of the injected dose, respectively. These results confirmed the long blood half-life of the PEG−TbNRs. As expected, an opposite trend was observed in the liver, showing 16.2 mg/kg of tissue at 1 h and 34.5 mg/kg of tissue at 24 h, respectively. Thus, the ICP results are in very good agreement with the CT and MRI results, demonstrating that PEG−TbNRs have long blood residence time, being still present at 24 h, and that they undergo slow hepatic clearance. Blood residence time is of utmost importance for some *in vivo* applications, in particular for tumor targeting. Efficient tumor targeting, whether passive, *via* enhanced permeability and retention (EPR) effect, or active, has been shown to require long circulation times.[45] Therefore, the ICP−MS results, which are in good agreement with the MRI findings and with the long-circulating nature of our PEG−TbNRs, further support the great potential of these nanosystems for *in vivo* applications, specifically for cancer imaging.

***In Vivo* Toxicity Assessment.** Finally, potential harm caused by the intravenous administration of PEG−TbNRs was assessed histologically and also by following the weight profile of the animals. H&E staining was carried out on tissue samples of the liver, kidneys, and spleen at 168 h postadministration of PEG−TbNRs. The liver sections of the animals injected with PEG−TbNRs resembled those injected with PBS. No evidence of acute and subacute liver injury, such as vacuolated swelling of the hepatocytes' cytoplasm, was observed in the liver sections (Figure S8). Likewise, no substantial changes were observed in the kidneys of the animals injected with PEG−TbNRs when compared to control animals. Kidneys exhibited regular intact brush borders and glomeruli around the Bowman's capsule (Figure S8).[46] Finally, the spleen also presented normal histological features with unaltered red and white pulp, which is characteristic of their normal architecture. Regarding the weight profile, a transient decrease in body weight was observed, with a maximum difference between groups at 24 h after the administration of PEG−TbNRs. However, after 168 h, the animals regained their normal weight, indicating the absence of toxic effects (Figure S9).
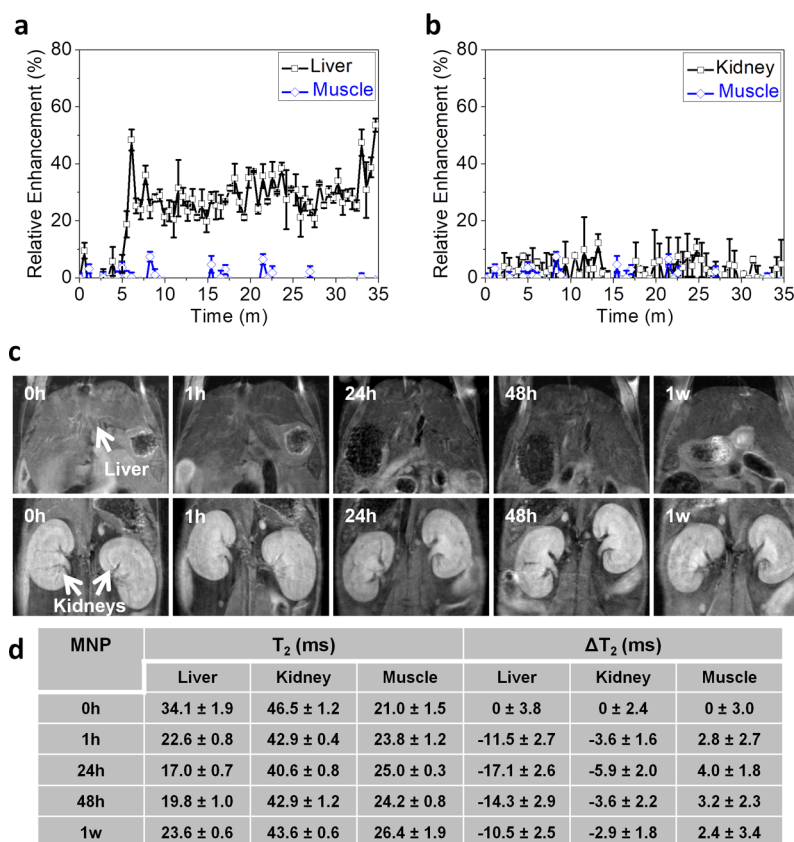
Figure 7. *In vivo* pharmacokinetics of intravenously injected PEG−TbNRs in BALB/c mice: (a) short-term pharmacokinetics in the liver; (b) short-term pharmacokinetics in the kidneys; (c) T_2-weighted MR images at different times postadministration of PEG-TbNRs; (d) T_2 variation in different tissues determined from *in vivo* T_2 maps (values correspond to average T_2 and ΔT_2 from 3 animals).

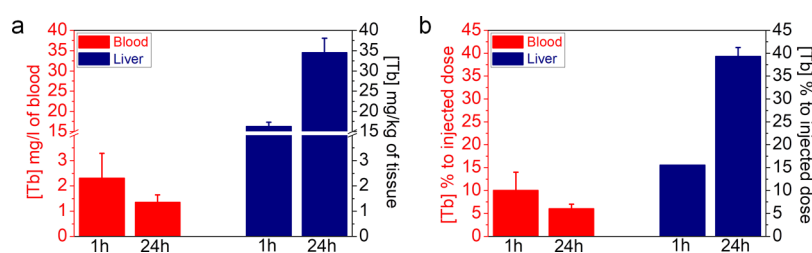| MNP	T_2 (ms)			ΔT_2 (ms)		
	Liver	Kidney	Muscle	Liver	Kidney	Muscle
0h	34.1 ± 1.9	46.5 ± 1.2	21.0 ± 1.5	0 ± 3.8	0 ± 2.4	0 ± 3.0
1h	22.6 ± 0.8	42.9 ± 0.4	23.8 ± 1.2	-11.5 ± 2.7	-3.6 ± 1.6	2.8 ± 2.7
24h	17.0 ± 0.7	40.6 ± 0.8	25.0 ± 0.3	-17.1 ± 2.6	-5.9 ± 2.0	4.0 ± 1.8
48h	19.8 ± 1.0	42.9 ± 1.2	24.2 ± 0.8	-14.3 ± 2.9	-3.6 ± 2.2	3.2 ± 2.3
1w	23.6 ± 0.6	43.6 ± 0.6	26.4 ± 1.9	-10.5 ± 2.5	-2.9 ± 1.8	2.4 ± 3.4

Figure 8. ICP−MS quantification of Tb content at 1 and 24 h post intravenous injection of PEG−TbNRs. (a) Absolute Tb concentration, (b) relative Tb concentration (% to the injected dose). Error bars correspond to standard deviation ($n = 3$).

■ CONCLUSIONS

We report the synthesis of PEGylated TbNRs with potential application as multimodal imaging CAs. TbNRs were synthesized by thermal decomposition of the as-prepared Tb−oleate. Then, TbNRs were successfully functionalized using a catechol-derived PEG ligand to render water-stable TbNRs. These PEG−TbNRs showed high colloidal stability in different media, absence of toxicity *in vitro* in cell cultures and *in vivo* in zebrafish embryos, and excellent properties as CT and MRI CAs. On the other hand, after intravenous injection in mice, the PEG−TbNRs showed excellent *in vivo* imaging contrast both in CT and MRI, long blood residence time, being still present after 24 h, and effective hepatic clearance. Altogether, these results demonstrate the high potential of PEG−TbNRs as *in vivo* multimodal CAs.

■ ASSOCIATED CONTENT

Ⓢ Supporting Information

The Supporting Information is available free of charge at https://pubs.acs.org/doi/10.1021/acsanm.1c00569.

> Details on the experimental section, TEM histograms, FTIR, DLS, UV−vis, PL, VSM, *in vitro* CT evaluation, magnetic relaxivity, *in vitro* cytotoxicity, *in vivo* toxicity, and *in vivo* side effects in rodents (PDF)

■ AUTHOR INFORMATION

Corresponding Authors

Manuel Pernia Leal − *Departamento de Química Orgánica y Farmacéutica, Facultad de Farmacia, Universidad de Sevilla, Seville 41012, Spain;* ⓞ orcid.org/0000-0001-8160-0574; Email: mpernia@us.es

María Luisa García-Martín − *BIONAND−Centro Andaluz de Nanomedicina y Biotecnología (Junta de Andalucía-*

Universidad de Málaga), Málaga 29590, Spain; Biomedical Research Networking Center in Bioengineering, Biomaterials & Nanomedicine (CIBER-BBN), Málaga 29590, Spain; orcid.org/0000-0002-2257-7682; Email: mlgarcia@bionand.es

Authors

Carlos Caro − *BIONAND−Centro Andaluz de Nanomedicina y Biotecnología (Junta de Andalucía-Universidad de Málaga), Málaga 29590, Spain;* orcid.org/0000-0003-4758-3816

Jose M. Paez-Muñoz − *BIONAND−Centro Andaluz de Nanomedicina y Biotecnología (Junta de Andalucía-Universidad de Málaga), Málaga 29590, Spain*

Ana M. Beltrán − *Departamento de Ingeniería y Ciencia de Los Materiales y Del Transporte, Escuela Politécnica Superior, Universidad de Sevilla, Sevilla 41011, Spain;* orcid.org/0000-0003-2599-5908

Complete contact information is available at:
https://pubs.acs.org/10.1021/acsanm.1c00569

Author Contributions

All authors contributed to the writing of the manuscript. The final version of the manuscript has been approved by all authors. C.C. and J.M.P.-M. contributed equally to this work.

Notes

The authors declare no competing financial interest.
The raw/processed data required to reproduce these findings cannot be shared at this time as the data also forms part of an ongoing study.

■ REFERENCES

(1) Runge, V. M.; Aoki, S.; Bradley, W. G., Jr.; Chang, K.-H.; Essig, M.; Ma, L.; Ross, J. S.; Valavanis, A. Magnetic Resonance Imaging and Computed Tomography of the Brain-50 Years of Innovation, With a Focus on the Future. *Invest. Radiol.* **2015**, *50*, 551−556.

(2) Campbell, B. C. V.; Christensen, S.; Levi, C. R.; Desmond, P. M.; Donnan, G. A.; Davis, S. M.; Parsons, M. W. Comparison of computed tomography perfusion and magnetic resonance imaging perfusion-diffusion mismatch in ischemic stroke. *Stroke* **2012**, *43*, 2648−2653.

(3) Xiao, Y.-D.; Paudel, R.; Liu, J.; Ma, C.; Zhang, Z.-S.; Zhou, S.-K. MRI contrast agents: Classification and application (Review). *Int. J. Mol. Med.* **2016**, *38*, 1319−1326.

(4) Wathen, C.; Foje, N.; Avermaete, T.; Miramontes, B.; Chapaman, S.; Sasser, T.; Kannan, R.; Gerstler, S.; Leevy, W. In vivo X-Ray Computed Tomographic Imaging of Soft Tissue with Native, Intravenous, or Oral Contrast. *Sensors* **2013**, *13*, 6957−6980.

(5) Lusic, H.; Grinstaff, M. W. X-ray-computed tomography contrast agents. *Chem. Rev.* **2013**, *113*, 1641−1666.

(6) McDonald, R. J.; McDonald, J. S.; Kallmes, D. F.; Jentoft, M. E.; Murray, D. L.; Thielen, K. R.; Williamson, E. E.; Eckel, L. J. Intracranial Gadolinium Deposition after Contrast-enhanced MR Imaging. *Radiology* **2015**, *275*, 772−782.

(7) Rogosnitzky, M.; Branch, S. Gadolinium-based contrast agent toxicity: a review of known and proposed mechanisms. *BioMetals* **2016**, *29*, 365−376.

(8) Ersoy, H.; Rybicki, F. J. Biochemical safety profiles of gadolinium-based extracellular contrast agents and nephrogenic systemic fibrosis. *J. Magn. Reson. Imag.* **2007**, *26*, 1190−1197.

(9) Cha, M. J.; Kang, D. Y.; Lee, W.; Yoon, S. H.; Choi, Y. H.; Byun, J. S.; Lee, J.; Kim, Y.-H.; Choo, K. S.; Cho, B. S.; Jeon, K. N.; Jung, J.-W.; Kang, H.-R. Hypersensitivity Reactions to Iodinated Contrast Media: A Multicenter Study of 196 081 Patients. *Radiology* **2019**, *293*, 117−124.

(10) Stacul, F.; van der Molen, A. J.; Reimer, P.; Webb, J. A.; Thomsen, H. S.; Morcos, S. K.; Almen, T.; Aspelin, P.; Bellin, M. F.; Clement, O.; Heinz-Peer, G. Contrast induced nephropathy: updated ESUR Contrast Media Safety Committee guidelines. *Eur. Radiol.* **2011**, *21*, 2527−2541.

(11) Attia, M. F.; Anton, N.; Akasov, R.; Chiper, M.; Markvicheva, E.; Vandamme, T. F. Biodistribution and Toxicity of X-Ray Iodinated Contrast Agent in Nano-emulsions in Function of Their Size. *Pharm. Res.* **2016**, *33*, 603−614.

(12) Roco, M. C.; Mirkin, C. A.; Hersam, M. C. Nanotechnology research directions for societal needs in 2020: summary of international study. *J. Nanoparticle Res.* **2011**, *13*, 897−919.

(13) Avasthi, A.; Caro, C.; Pozo-Torres, E.; Leal, M. P.; García-Martín, M. L. Magnetic Nanoparticles as MRI Contrast Agents. *Top. Curr. Chem.* **2020**, *378*, 40.

(14) Lee, N.; Choi, S. H.; Hyeon, T. Nano-sized CT contrast agents. *Adv. Mater.* **2013**, *25*, 2641−2660.

(15) Escudero, A.; Becerro, A. I.; Carrillo-Carrión, C.; Núñez, N. O.; Zyuzin, M. V.; Laguna, M.; González-Mancebo, D.; Ocaña, M.; Parak, W. J. Rare earth based nanostructured materials: synthesis, functionalization, properties and bioimaging and biosensing applications. *Nanophotonics* **2017**, *6*, 881.

(16) Tian, Y.; Yang, H.-Y.; Li, K.; Jin, X. Monodispersed ultrathin GdF3 nanowires: oriented attachment, luminescence, and relaxivity for MRI contrast agents. *J. Mater. Chem.* **2012**, *22*, 22510−22516.

(17) Zairov, R.; Khakimullina, G.; Podyachev, S.; Nizameev, I.; Safiullin, G.; Amirov, R.; Vomiero, A.; Mustafina, A. Hydration number: crucial role in nuclear magnetic relaxivity of Gd(III) chelate-based nanoparticles. *Sci. Rep.* **2017**, *7*, 14010.

(18) Kang, X.; Yang, D.; Ma, P.; Dai, Y.; Shang, M.; Geng, D.; Cheng, Z.; Lin, J. Fabrication of Hollow and Porous Structured GdVO4:Dy3+ Nanospheres as Anticancer Drug Carrier and MRI Contrast Agent. *Langmuir* **2013**, *29*, 1286−1294.

(19) Zairov, R.; Pizzanelli, S.; Dovzhenko, A. P.; Nizameev, I.; Orekhov, A.; Arkharova, N.; Podyachev, S. N.; Sudakova, S.; Mustafina, A. R.; Calucci, L. Paramagnetic Relaxation Enhancement in Hydrophilic Colloids Based on Gd(III) Complexes with Tetrathia- and Calix[4]arenes. *J. Phys. Chem. C* **2020**, *124*, 4320−4329.

(20) González-Mancebo, D.; Becerro, A. I.; Rojas, T. C.; García-Martín, M. L.; de la Fuente, J. M.; Ocaña, M. HoF3 and DyF3 Nanoparticles as Contrast Agents for High-Field Magnetic Resonance Imaging. *Part. Part. Syst. Char.* **2017**, *34*, 1700116.

(21) Groman, E. V.; Bouchard, J. C.; Reinhardt, C. P.; Vaccaro, D. E. Ultrasmall mixed ferrite colloids as multidimensional magnetic

resonance imaging, cell labeling, and cell sorting agents. *Bioconjugate Chem.* **2007**, *18*, 1763−1771.

(22) Chen, F.; Chen, M.; Yang, C.; Liu, J.; Luo, N.; Yang, G.; Chen, D.; Li, L. Terbium-doped gadolinium oxide nanoparticles prepared by laser ablation in liquid for use as a fluorescence and magnetic resonance imaging dual-modal contrast agent. *Phys. Chem. Chem. Phys.* **2015**, *17*, 1189−1196.

(23) Biju, V.; Hamada, M.; Ono, K.; Sugino, S.; Ohnishi, T.; Shibu, E. S.; Yamamura, S.; Sawada, M.; Nakanishi, S.; Shigeri, Y.; Wakida, S.-i. Nanoparticles speckled by ready-to-conjugate lanthanide complexes for multimodal imaging. *Nanoscale* **2015**, *7*, 14829−14837.

(24) Liu, K.; Shi, X.; Wang, T.; Ai, P.; Gu, W.; Ye, L. Terbium-doped manganese carbonate nanoparticles with intrinsic photo-luminescence and magnetic resonance imaging capacity. *J. Colloid Interface Sci.* **2017**, *485*, 25−31.

(25) González-Mancebo, D.; Becerro, A. I.; Corral, A.; García-Embid, S.; Balcerzyk, M.; Garcia-Martin, M. L.; de la Fuente, J. M.; Ocana, M. Design of a nanoprobe for high field magnetic resonance imaging, dual energy X-ray computed tomography and luminescent imaging. *J. Colloid Interface Sci.* **2020**, *573*, 278−286.

(26) Ocaña, M.; Nuñez, N. O.; Becerro, A. I.; Lozano, G.; Moros, M.; de la Fuente, J. M.; Corral, A.; Balcerzyk, M.; Ocana, M. Synthesis, functionalization and properties of uniform europium-doped sodium lanthanum tungstate and molybdate (NaLa(XO4)2, X=Mo,W) probes for luminescent and X-ray computed tomography bioimaging. *J. Colloid Interface Sci.* **2019**, *554*, 520−530.

(27) Ocaña, A.; Vidal-Moya, A.; Bernabeu, A.; Pacheco-Torres, J.; Checa-Chavarria, E.; Fernández, E.; Botella, P. Gd-Si Oxide Nanoparticles as Contrast Agents in Magnetic Resonance Imaging. *Nanomaterials (Basel)* **2016**, *6*, 109.

(28) Miao, X.; Ho, S. L.; Tegafaw, T.; Cha, H.; Chang, Y.; Oh, I. T.; Yaseen, A. M.; Marasini, S.; Ghazanfari, A.; Yue, H.; Chae, K. S.; Lee, G. H. Stable and non-toxic ultrasmall gadolinium oxide nanoparticle colloids (coating material = polyacrylic acid) as high-performance T1 magnetic resonance imaging contrast agents. *RSC Adv.* **2018**, *8*, 3189−3197.

(29) Zhao, Z.; Xu, K.; Fu, C.; Liu, H.; Lei, M.; Bao, J.; Fu, A.; Yu, Y.; Zhang, W. Interfacial engineered gadolinium oxide nanoparticles for magnetic resonance imaging guided microenvironment-mediated synergetic chemodynamic/photothermal therapy. *Biomaterials* **2019**, *219*, 119379.

(30) Bony, B. A.; Miller, H. A.; Tarudji, A. W.; Gee, C. C.; Sarella, A.; Nichols, M. G.; Kievit, F. M. Ultrasmall Mixed Eu−Gd Oxide Nanoparticles for Multimodal Fluorescence and Magnetic Resonance Imaging of Passive Accumulation and Retention in TBI. *ACS Omega* **2020**, *5*, 16220−16227.

(31) Marasini, S.; Yue, H.; Ho, S. L.; Jung, K.-H.; Park, J. A.; Cha, H.; Ghazanfari, A.; Ahmad, M. Y.; Liu, S.; Jang, Y. J.; Miao, X.; Chae, K.-S.; Chang, Y.; Lee, G. H. d-Glucuronic Acid-Coated Ultrasmall Paramagnetic Ln2O3 (Ln = Tb, Dy, and Ho) Nanoparticles: Magnetic Properties, Water Proton Relaxivities, and Fluorescence Properties. *Eur. J. Inorg. Chem.* **2019**, *2019*, 3832−3839.

(32) Yi, Z.; Li, X.; Lu, W.; Liu, H.; Zeng, S.; Hao, J. Hybrid lanthanide nanoparticles as a new class of binary contrast agents for in vivo T1/T2 dual-weighted MRI and synergistic tumor diagnosis. *J. Mater. Chem. B* **2016**, *4*, 2715−2722.

(33) Pernia Leal, M.; Rivera-Fernández, S.; Franco, J. M.; Pozo, D.; de la Fuente, J. M.; García-Martín, M. L. Long-circulating PEGylated manganese ferrite nanoparticles for MRI-based molecular imaging. *Nanoscale* **2015**, *7*, 2050−2059.

(34) Caro, C.; Carmen Muñoz-Hernández, M.; Leal, M. P.; García-Martín, M. L. In Vivo Pharmacokinetics of Magnetic Nanoparticles. *Methods Mol. Biol.* **2018**, *1718*, 409−419.

(35) Pernia Leal, M.; Caro, C.; García-Martín, M. L. Shedding light on zwitterionic magnetic nanoparticles: limitations for in vivo applications. *Nanoscale* **2017**, *9*, 8176−8184.

(36) Pozo-Torres, E.; Caro, C.; Avasthi, A.; Páez-Muñoz, J. M.; García-Martín, M. L.; Fernández, I.; Pernia Leal, M. Clickable iron oxide NPs based on catechol derived ligands: synthesis and characterization. *Soft Matter* **2020**, *16*, 3257−3266.

(37) Heffern, M. C.; Matosziuk, L. M.; Meade, T. J. Lanthanide probes for bioresponsive imaging. *Chem. Rev.* **2014**, *114*, 4496−4539.

(38) Di Bernardo, P.; Zanonato, P. L.; Bismondo, A.; Melchior, A.; Tolazzi, M. Protonation and lanthanide(III) complexation equilibria of a new tripodal polyaza-polycatechol-amine. *Dalton Trans.* **2009**, 4236−4244.

(39) Tang, Q.; Shen, J.; Zhou, W.; Zhang, W.; Yu, W.; Qian, Y. Preparation, characterization and optical properties of terbium oxide nanotubes. *J. Mater. Chem.* **2003**, *13*, 3103−3106.

(40) Caro, C.; Dalmases, M.; Figuerola, A.; García-Martín, M. L.; Leal, M. P. Highly water-stable rare ternary Ag-Au-Se nanocomposites as long blood circulation time X-ray computed tomography contrast agents. *Nanoscale* **2017**, *9*, 7242−7251.

(41) Jun, Y. W.; Kim, H. R.; Reo, Y. J.; Dai, M.; Ahn, K. H. Addressing the autofluorescence issue in deep tissue imaging by two-photon microscopy: the significance of far-red emitting dyes. *Chem. Sci.* **2017**, *8*, 7696−7704.

(42) Caro, C.; Egea-Benavente, D.; Polvillo, R.; Royo, J. L.; Pernia Leal, M.; García-Martín, M. L. Comprehensive Toxicity Assessment of PEGylated Magnetic Nanoparticles for in vivo applications. *Colloids Surf. B Biointerfaces* **2019**, *177*, 253−259.

(43) Guo, Y.; Chen, L.; Wu, J.; Hua, J.; Yang, L.; Wang, Q.; Zhang, W.; Lee, J.-S.; Zhou, B. Parental co-exposure to bisphenol A and nano-TiO2 causes thyroid endocrine disruption and developmental neurotoxicity in zebrafish offspring. *Sci. Total Environ.* **2019**, *650*, 557−565.

(44) Xiao, Y.; Zeng, G.; Liu, X.; Peng, C.; Lai, C.; Zhou, P. Safety enhancement in adult body computed tomography scanning: comparison of iodixanol versus iohexol. *Springerplus* **2016**, *5*, 148.

(45) Perrault, S. D.; Walkey, C.; Jennings, T.; Fischer, H. C.; Chan, W. C. W. Mediating tumor targeting efficiency of nanoparticles through design. *Nano Lett.* **2009**, *9*, 1909−1915.

(46) Peter, A. I.; Naidu, E. C.; Akang, E.; Ogedengbe, O. O.; Offor, U.; Rambharose, S.; Kalhapure, R.; Chuturgoon, A.; Govender, T.; Azu, O. O. Investigating Organ Toxicity Profile of Tenofovir and Tenofovir Nanoparticle on the Liver and Kidney: Experimental Animal Study. *Toxicol. Res.* **2018**, *34*, 221−229.